Synthesis, Lithium Insertion and Thermal Stability of Si–Mo Alloys

Journal of The Electrochemical Society, 2020 **167** 130531

Synthesis, Lithium Insertion and Thermal Stability of Si–Mo Alloys

Simeng Cao,[1] Shayne Gracious,[1] J. Craig Bennett,[2] and M. N. Obrovac[1,3,*,z]

[1]*Department of Chemistry, Dalhousie University, Halifax, N.S. B3H 4R2, Canada*
[2]*Department of Physics, Acadia University, Wolfville, N.S. B4P 2R6, Canada*
[3]*Department of Physics and Atmospheric Science, Dalhousie University, Halifax, N. S. B3H 4R2, Canada*

Li insertion was investigated in Si_xMo_{100-x} ($90 \geqslant x \geqslant 70$, $\Delta x = 10$) alloys prepared by mechanical ball milling. X-ray diffraction (XRD) and quantitative phase analysis were used to analyze phase compositions of these Si–Mo alloys, and how these phase compositions changed with milling times. The results of quantitative phase analysis showed that cr-Si converted into a-Si within 1 h during milling, and the Si–Mo reactions were nearly complete after only 4-h milling. During electrochemical cycling, the Si–Mo samples with high initial Mo contents and long milling times displayed good crystalline $Li_{15}Si_4$ suppression and stable cycling performance. In addition, thermal stability of some selected Si–Mo alloys was studied. The $Si_{80}Mo_{20}$ 16 h alloy combines good thermal stability and a high volumetric capacity of about 1300–1400 Ah L^{-1} after heat treatment at 600 °C or 800 °C, which may allow the alloy to be further improved by carbon coating at high temperature.

 [DOI: 10.1149/1945-7111/abba91]

Manuscript submitted July 15, 2020; revised manuscript received September 14, 2020. Published October 5, 2020.

Supplementary material for this article is available online

Graphite is an excellent anode material, and has been used widely for lithium batteries, due to its low cost, abundance, good electronic conductivity, good cycle life, low average potential (0.125 V vs Li/Li^+), and low volume expansion during lithiation (~10%).[1,2] However, the volumetric capacity of graphite is limited to about 760 Ah L^{-1}.[2] To enable cells with higher energy densities, other anode materials have been studied, such as Si and Sn.[3,4] Si has the highest volumetric capacity (2194 Ah L^{-1}) among all known Li storage materials, and it also has a low average potential (~0.4 V vs Li/Li^+).[1] In a full cell model considering the impact of anode average potential on cell energy density, Si can provide an additional 34% volumetric energy density compared to graphite.[1] However, Si experiences a huge volume expansion/contraction during lithiation/delithiation, and the volume expansion can reach up to approximately 280% after full lithiation.[3] The repeated volume changes of Si during cell cycling are not only detrimental to Si anode structural stability, but also result in exposure of more fresh Si surfaces to electrolyte, resulting in continual electrolyte decomposition and solid electrolyte interphase (SEI) growth. In addition, the formation of crystalline $Li_{15}Si_4$ (cr-$Li_{15}Si_4$) when Si is fully lithiated is thought to lead to capacity fade.[5] These issues (volume expansion of Si during lithiation, electrolyte reactivity, and cr-$Li_{15}Si_4$ formation) can significantly reduce Si anode lifetime. During the last several decades, extensive research has been conducted to solve these issues.[3,6,7]

Preparing Si/inactive alloys is regarded as an efficient way to relieve the problems mentioned above. When Si particles are dispersed in an inactive matrix, the total volume expansion after lithiation can be diluted.[8] It has also been found that incorporating inactive phases in Si alloys can suppress cr-$Li_{15}Si_4$ formation.[9,10] In addition, Si/inactive alloys can provide volumetric energy density improvement over pure Si at a given volume expansion.[8] A Si/inactive anode material is typically synthesized by alloying Si with one or more transition metal elements via sputter deposition or mechanical milling, resulting in amorphous/nanostructured alloys that consist of transition metal silicide and active Si phases.[9,11,12] Most silicides are electrochemically inactive in Li-ion cells at room temperature.[13,14] However, there are exceptions. For example, Du et al. revealed that nanocrystalline $NiSi_2$ has electrochemical activity with Li, although bulk crystalline $NiSi_2$ was inactive during 30 °C cycling.[15]

Si-based alloys can be further modified by carbon coating. Carbon coating improves cycle life, due to the good electrical conductivity of carbon and by providing a protective barrier to reduce reactions with electrolyte.[16,17] Chemical vapor deposition (CVD) is an important method to apply carbon coatings to Si-based anode materials.[18] However, CVD coating is a high temperature process, requiring samples to be heated to at least 800 °C for a pure carbon phase to be deposited. This is problematic for nanostructured Si alloys and Si/C composites, since amorphous Si crystallizes at temperatures of 600 °C, resulting in the growth of large crystalline Si grains. This is detrimental for Si-based anode materials, since it is desirable that the active Si phase be amorphous or nanocrystalline (e.g. < 150 nm), otherwise fracture of the active Si phase can occur during cycling, resulting in capacity fade.[19,20] Therefore, Si alloys with high thermal stability against grain growth are highly desirable.

In this study, the synthesis, electrochemistry, and thermal stability of Si/Mo alloys were investigated. To our knowledge, lithium insertion in these alloys has not been investigated previously. Their propensity to form nanostructured alloys during ball milling was evaluated, as it is commercially important that precursors used for ball milling processes be amenable towards rapid alloy formation. The thermal stability of the resulting nanostructured Si/Mo alloys was also investigated. It was hoped that the high melting point of the $MoSi_2$ inactive phase (2020 °C) would impart thermal stability onto nanostructured Si/Mo alloys, so that these alloys could be compatible with high-temperature post-processing methods (e.g. CVD processing). Finally, an electrochemical investigation of Si–Mo alloys as-milled and after heat treatment was done to studying their potential as anode materials.

Experimental

Si_xMo_{100-x} ($90 \geqslant x \geqslant 70$, $\Delta x = 10$) samples were prepared by ball milling according to a method optimized in a previous study.[21] A total of 0.5 ml of Si powder (Sigma-Aldrich, 325 mesh, 99%) and Mo powder (Alfa Aesar, 250 mesh, 99.9%) in different stoichiometric ratios were loaded into ball milling containers (SPEX CertiPrep, 65 ml hardened steel) with 180 g of stainless steel balls (d = 1/16 inch (1.6 mm)). Containers were flushed with argon and sealed in an Ar-filled glovebox and then placed in a high energy ball

*Electrochemical Society Member.
[z]E-mail: mnobrovac@dal.ca

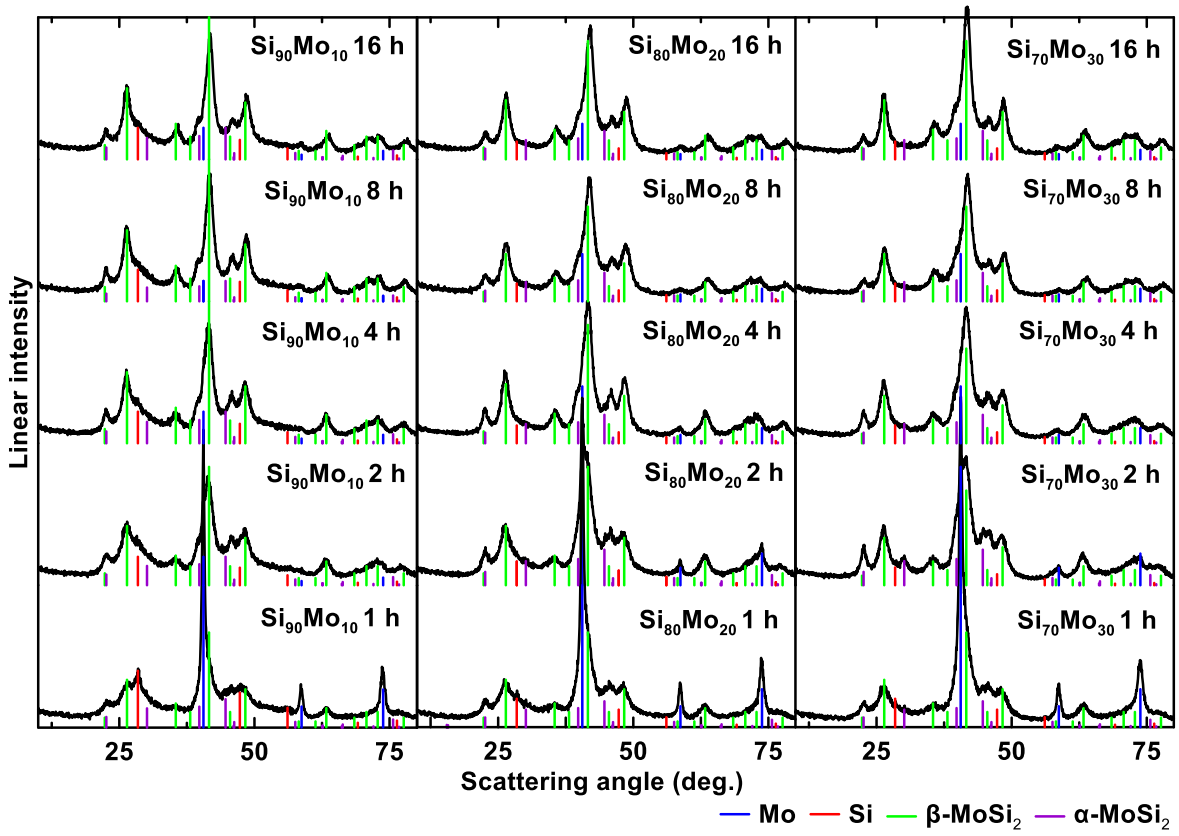

Figure 1. XRD patterns of Si_xMo_{100-x} alloys made with different compositions and milling times.

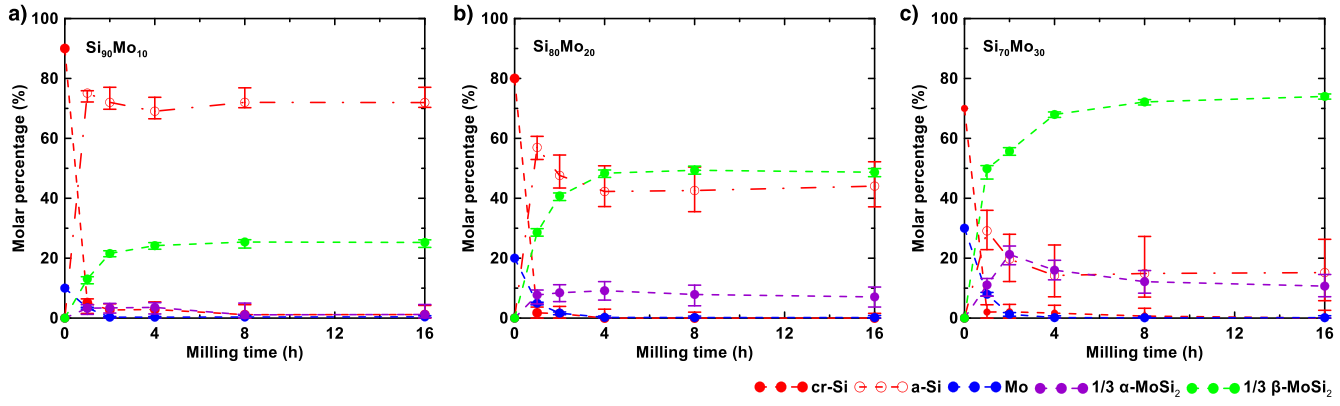

Figure 2. Phase composition analysis of Si–Mo alloys made with different milling times: (a) $Si_{90}Mo_{10}$; (b) $Si_{80}Mo_{20}$; (c) $Si_{70}Mo_{30}$. All molar percentages are calculated on a per atom basis.

mill (SPEX CertiPrep 8000) for 1–16 h. After milling, about 20 ml of ethanol was added to the container, and the mixture was milled for another 5 min in air. The ethanol/sample slurry was removed, and the sample was obtained by drying in air. In addition, Si powder (Sigma-Aldrich, 325 mesh, 99%), Mo powder (Alfa Aesar, 250 mesh, 99.9%), and α-$MoSi_2$ (Sigma-Aldrich, 7.5 μm, 99.8%) were ball milled under the same conditions for 2 h. In some instances, caking of the sample on the inner wall of the container occurred. When this occurred, the caked portion of the sample was collected by milling with ethanol and several 1/4 inch (6.35 mm) stainless steel balls.

Selected ball milled Si_xMo_{100-x} (1, 4 and 16 h) samples were heated in a tube furnace under flowing argon. The temperature of the furnace was increased from room temperature at a heating rate of 10 °C min^{-1}, to a target temperature of 600 °C or 800 °C. This temperature was then maintained for 3 h. The samples were then naturally cooled to room temperature under argon flow.

Selected Si–Mo samples were characterized with a Schottky field emission scanning electron microscope (SEM, TESCAN MIRA 3 LMU) using a 20.0 kV accelerating voltage. Si–Mo sample densities were measured with a Micromeritics AccuPyc II 1340 gas pycnometer. Transmission electron microscopy (TEM), selected area electron diffraction (SAED), and high-resolution electron microscopy (HREM) images were collected using a Philips CM30 TEM with an operating voltage of 250 kV. TEM specimens were prepared by suspending Si–Mo alloy powders in methanol, sonicating about 10 min, and placing a drop onto lacey carbon coated TEM grid. Element (Si and Mo) distributions in single particles of Si–Mo samples were investigated by elemental mapping. The data was collected in scanning TEM mode (STEM). A nominal analytical

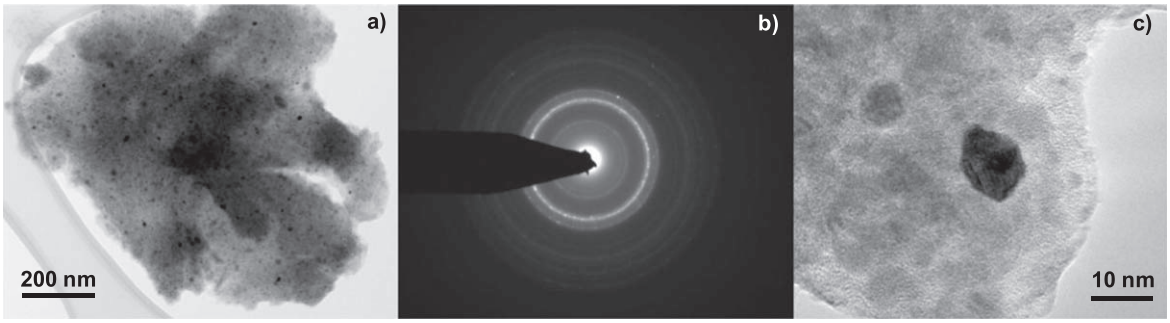

Figure 3. TEM images of $Si_{80}Mo_{20}$ (8 h): (a) BF image, (b) SAED pattern, and (c) HREM image.

beam diameter of 1 nm was used at 200 kV, where the dwell time was 100 μs. X-ray diffraction (XRD) patterns of Si–Mo alloys were collected using a Rigaku Ultima IV diffractometer with a Cu Kα X-ray source, a diffracted beam monochromator, and a scintillation counter detector. XRD patterns were collected in the range of 10° ∼ 80° 2θ in 0.05° increments for 3 s per step. For air sensitive samples, the powders were sealed in a gas-tight sample holder with an aluminized Mylar™ window under Ar atmosphere.

Phases observed in XRD patterns of Si–Mo samples were quantitatively analyzed using the 100% approach, according to Eq. 1.[22]

$$X_i = \frac{I_i/IF_i}{\sum_1^n I_i/IF_i} \quad [1]$$

Where X_i is mass percentage of phase i in a Si–Mo sample, and I_i is integrated intensity of phase i in the XRD scan of the sample. IF_i is the intensity factor value of phase i, according to:

$$IF_i = \frac{I_i' X_s}{I_s X_i'} \quad [2]$$

Where X_i' is the mass percentage of phase i in a mixture of phase i and an internal standard (IS), I_i' is the integrated intensity of phase i in the XRD pattern of the mixture, and X_s and I_s are the mass percentage and integrated intensity of the IS in the mixture, respectively. Here TiN (Alfa Aesar, 200 mesh, 99.5%) was used as the IS. More detailed information about the method can be found in Refs. 22 and 23.

Electrodes were prepared from slurries comprising a mixture of Si–Mo alloy, carbon black (Super C65, Timcal), 10 weight % aqueous solution of lithium polyacrylate (LiPAA) (made by neutralizing a polyacrylic acid solution (Sigma-Aldrich, average molecular weight ∼250,000 g mol^{-1})), a wetting agent (isopropanol, Sigma-Aldrich, 99.5%), and distilled water. The volume ratio of the Si–Mo alloy, Super C, and LiPAA was 70:5:25. The mixture was dispersed using a planetary mill (Retsch, PM200) with 3 tungsten carbide balls (d = 7/16 inch, about 11.1 mm) at 100 rpm for 1 h. The mixed electrode slurry was spread onto copper foil (Furukawa Electric, Japan) using a stainless steel coating bar with a 0.004-inch gap, and the coating was dried in air at 120 °C for 1 h. The typical mass loadings of electrodes were 2 ∼ 3 mg cm^{-2}, which corresponds to an area specific capacity of ∼2 mAh cm^{-2}. These low electrode loadings were purposely used to evaluate the alloy electrochemistry, while minimizing the effects coating or binder performance.

Disk electrodes (13 mm in diameter) were cut from the dried coatings with an electrode punch and were further dried under vacuum at 120 °C for 2 h before cell assembly. 2325-type coin cells were assembled in an Ar filled glovebox with a prepared electrode as the working electrode, lithium metal (99.9%, Sigma-Aldrich) as a counter/reference electrode, and with two Celgard 2300 separators. A solution of 1 M $LiPF_6$ (BASF, 98%) in ethylene carbonate (EC)/diethyl carbonate (DEC)/monofluoroethylene carbonate (FEC) in a volume ratio of 3:6:1 (all from BASF) was used as electrolyte. Cells were cycled between 0.005–0.9 V at 30.0 ± 0.1 °C using a battery testing system (Neware). To determine cycling rates, trial cells for Si–Mo alloys were cycled at a C/20 rate, assuming that all the Si in the alloy was active with a capacity of 3578 mAh g^{-1}. The actual material capacities were then obtained from the trial cell measured capacities. These experimentally derived capacities were then used to determine the cycling rates for Si–Mo alloy cells used for cycling experiments. During the first cycle, cells were discharged (alloy lithiation) at a constant C/20 rate to 0.005 V. After that, the cells were also discharged at C/30 and C/40 rates with a 10 min open-circuit period between current steps once the cutoff potential (0.005 V) had been reached, in order to simulate CCCV cycling in full cells. Subsequently, the cells were charged at C/20 rate to 0.9 V. All C-rates employed during the first cycle were doubled in the following cycles.

Results and Discussion

Backscattered electron (BSE) images of several Si–Mo samples ($Si_{90}Mo_{10}$ 1 h, $Si_{90}Mo_{10}$ 16 h, $Si_{70}Mo_{30}$ 1 h, and $Si_{70}Mo_{30}$ 16 h) are shown in Fig. S1 (available online at stacks.iop.org/JES/167/130531/mmedia). Bright spots in the samples milled for 1 h indicate the presence of unmilled Mo particles. The samples become more homogeneous as milling time is increased. No Mo particles are present after 16 h milling. XRD patterns of Si_xMo_{100-x} alloys (90 ⩾ x ⩾ 70, Δx = 10, milling time: 1–16 h) are shown in Fig. 1. These Si–Mo alloys are composed of crystalline Si (cr-Si), amorphous Si (a-Si), Mo, and nanocrystalline α and β-$MoSi_2$ phases. The large width of the a-Si peaks makes them difficult to discern in some XRD patterns. Mo and cr-Si peaks are significant at low milling times, but their peaks decrease in intensity as Mo and Si react during milling to form $MoSi_2$. According to the Si–Mo equilibrium phase diagram,[24] α-$MoSi_2$ is a the low temperature form of this phase, with an α-$MoSi_2$/Si 2-phase region present below 1400 °C. Above 1900 °C the α-$MoSi_2$ phase converts to β-$MoSi_2$. It is interesting that the high-temperature β-$MoSi_2$ phase was the main silicide produced during milling. Only a small amount of α-$MoSi_2$ formed. This illustrates that ball milling is a non-equilibrium process that often produces metastable phases.

The evolution of the phase compositions of the Si–Mo alloys during ball milling was determined quantitatively from XRD measurements, as described in the Supporting Information, and the results are shown in Fig. 2. For all the samples, cr-Si converts to a-Si within 1 h of milling. Concurrently, Si reacts with Mo to form α-$MoSi_2$ or β-$MoSi_2$. This reaction is slower and takes about 4 h to reach completion. However, nearly all of the Mo was consumed after only about 2 h, which conflicts with the completed reaction time (4 h), as indicated by when the reaction reaches steady-state. The rapid disappearance of Mo in the XRD patterns is likely due to it adhering to the wall of the milling vial, as is discussed below. Alloys with more Mo content produced a higher fraction of α-$MoSi_2$ during milling. Some of the α-$MoSi_2$ converted into β-$MoSi_2$ with longer

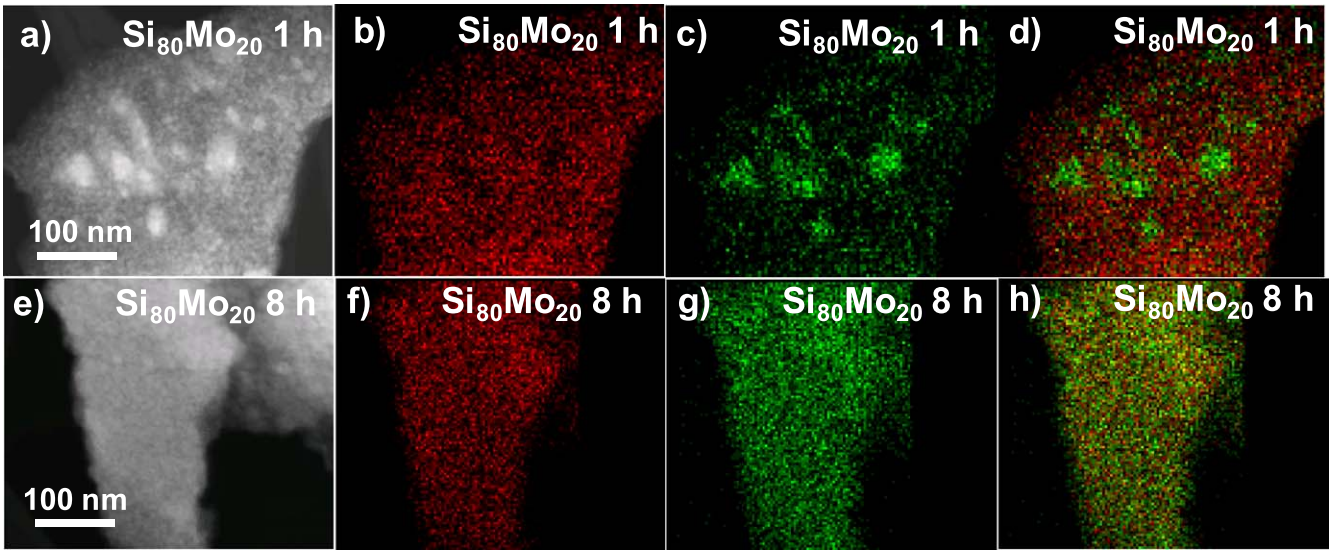

Figure 4. STEM images, Si maps, Mo maps, and Si–Mo substitution overlays, respectively, of $Si_{80}Mo_{20}$ alloy made with 1 h milling time (a)–(d) and 8 h milling time (e)–(h). (red = Si, green = Mo).

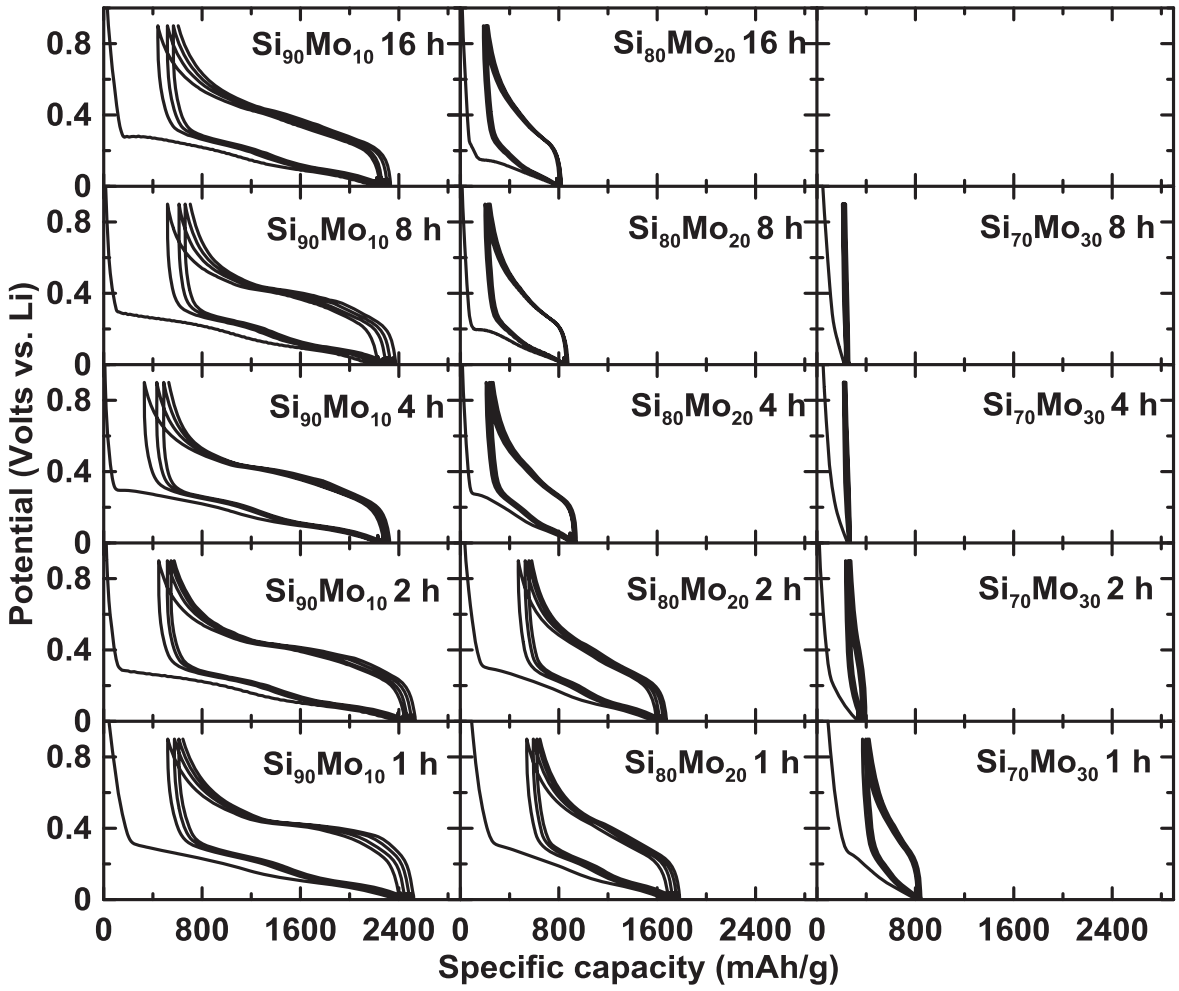

Figure 5. Potential profiles of Si_xMo_{100-x} ($90 \geqslant x \geqslant 70$, $\Delta x = 10$, 1–16 h) alloy electrodes vs Li.

milling time. Based on the Scherrer equation, the grain size of the β-$MoSi_2$ phase was estimated to be about 3 nm in size for all samples as it was initially formed and increased to 4 nm with longer milling time. It is possible that as more β-$MoSi_2$ is formed, there is a greater chance of aggregation of this phase and therefore a greater chance of producing larger grains.

As mentioned above, the Mo metal phase content is nearly zero after 2 h milling, however a few percent Mo remains for the entire

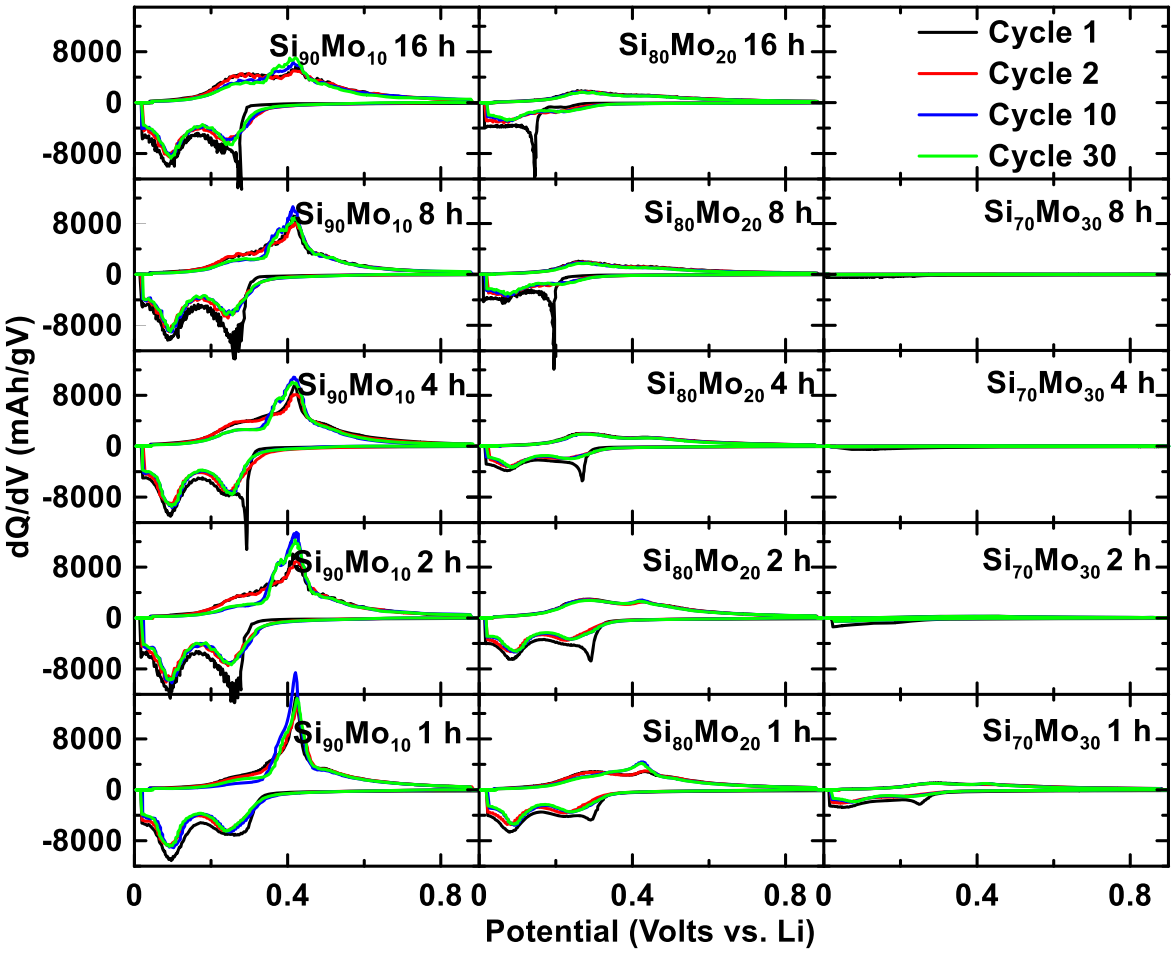

Figure 6. Differential capacity curves of Si_xMo_{100-x} ($90 \geqslant x \geqslant 70$, $\Delta x = 10$, 1–16 h) alloy electrodes.

duration of milling. This may be indicative that Mo is adhering to the interior walls of the ball mill vial during milling. This would cause the Mo content in the collected powder to rapidly decrease. At the same time, the Mo adhered to the walls may be constantly eroding off during the milling process, resulting in a few percent Mo content in the collected powder at all times. To confirm this, Si and Mo powders with a stoichiometric ratio of 70:30 were milled for either 1 h or 16 h. In each case, the loose powder and the powder scraped off the walls (the "cake") were collected. Their XRD patterns are shown in Fig. S3a. For the $Si_{70}Mo_{30}$ 1 h or 16 h samples, the XRD patterns typically consist of Mo, β-$MoSi_2$, a-Si, cr-Si, and possibly some α-$MoSi_2$. However, the relative peak areas of each phase in the cake and loose powder differ significantly. Results of a quantitative phase analysis of these XRD patterns are shown in Fig. S3b. In both samples, the cake formed on the interior vial wall is significantly richer in Mo and poorer in $MoSi_2$ than the collected loose powder. This result suggests that Mo has a higher tendency than the other phases present to cake during milling, resulting in compositional segregation during milling. This explains the fast Mo depletion during milling shown in Fig. 2. This effect has been shown previously to occur for Si–W alloys.[25] It can be also observed from Fig. S3b that the Mo phase content in the cake decreases with longer milling time. This suggests that Mo can be eroded from the walls during milling, resulting in a constant few percent Mo observed during all phases of milling. The propensity for Mo to form a cake on the side of the milling vial may make Si–Mo alloys difficult to scale up.

TEM results for Si–Mo alloys with complete reactions are generally the same. TEM images of the $Si_{80}Mo_{20}$ (8 h) alloy are shown in Fig. 3, including a bright field (BF) image (Fig. 3a), a SAED pattern (Fig. 3b), and a HREM image (Fig. 3c). All the diffraction rings observed in Fig. 3b correspond to the lattice spacings of β-$MoSi_2$, which are fairly continuous and intense, indicating a significant amount of nanocrystalline β-$MoSi_2$ is present in this alloy, consistent with the most intense phase observed in XRD patterns. The diffuse rings in the SAED pattern are typical of a-Si. Based on TEM images, the Si–Mo alloys consist of β-$MoSi_2$ nanocrystals with a grain size of about 5–10 nm that are homogeneously embedded in an a-Si matrix.

Si and Mo distributions in single particles of the $Si_{80}Mo_{20}$ (1 h and 8 h) samples were investigated by X-ray compositional mapping. STEM images, Si maps, Mo maps, and Si–Mo substitution overlays are exhibited in Figs. 4a and 4e, 4b and 4f, 4c and 4g, and 4d and 4h, for 1 h and 8 h milled samples, respectively. The substitution overlays are employed to show a combination of Si and Mo elements, where only the element with the highest intensity at each pixel is displayed. The results indicate that the $Si_{80}Mo_{20}$ (8 h) alloy has a more homogeneous Si–Mo distribution than the $Si_{80}Mo_{20}$ (1 h) alloy. This phenomenon is typical of all the Si–Mo samples with different Si–Mo stoichiometric ratios studied here.

The first four cycles of the Si_xMo_{100-x} ($90 \geqslant x \geqslant 70$, $\Delta x = 10$, 1–16 h) half-cell potential profiles are shown in Fig. 5. Generally, the potential profiles of $Si_{90}Mo_{10}$ (1–16 h), $Si_{80}Mo_{20}$ (1–16 h), and $Si_{70}Mo_{30}$ (1 h) samples have characteristics typical of a-Si, namely two sloping plateaus during the lithiation processes.[26] A plateau at about 0.45 V can also be observed in the delithiation potential profiles of $Si_{90}Mo_{10}$ (1–8 h), which is from cr-$Li_{15}Si_4$ delithiation and indicates cr-$Li_{15}Si_4$ formation during lithiation.[27] The reversible and irreversible specific capacities and initial columbic efficiencies (ICE) of the Si_xMo_{100-x} samples are listed in Table SI, respectively.

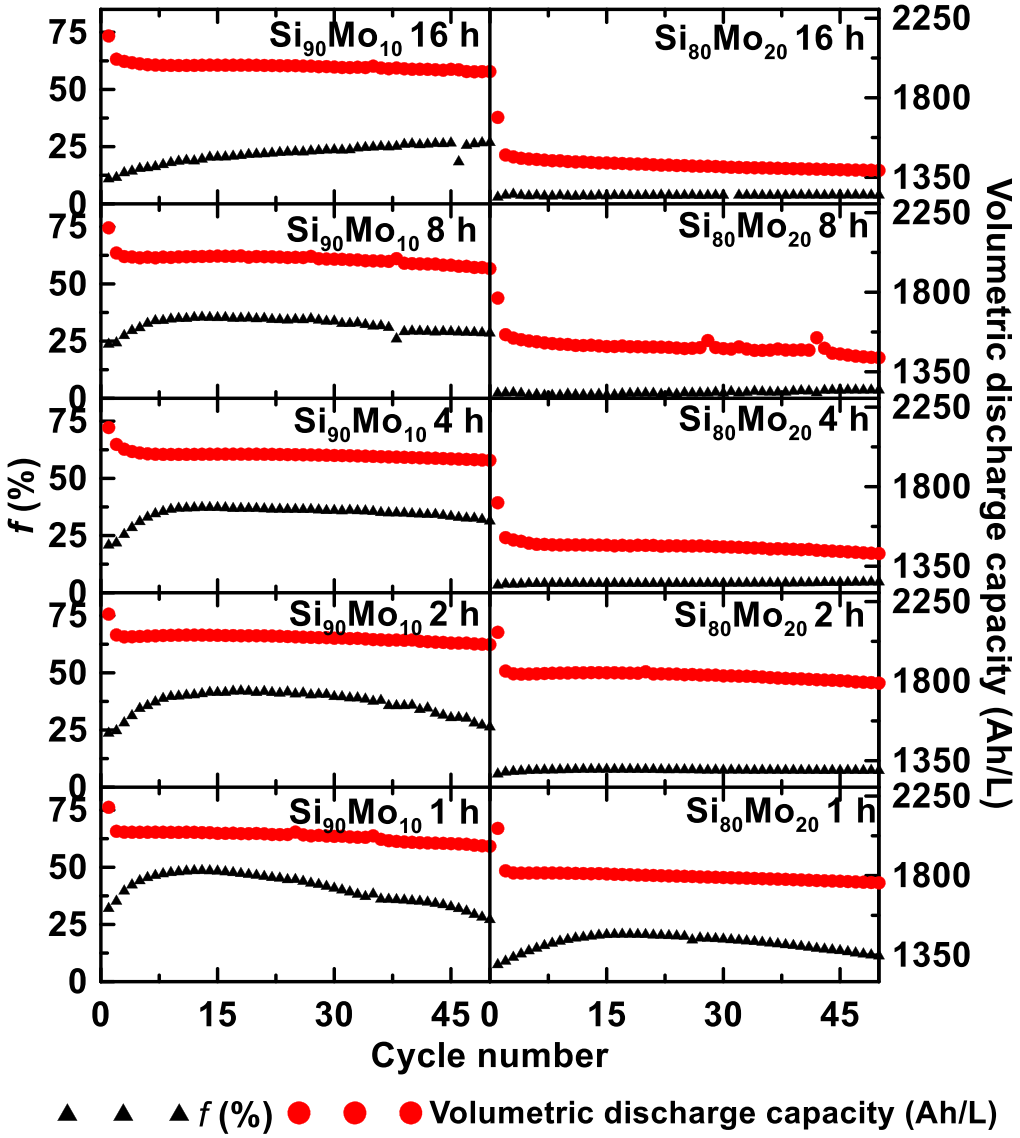

Figure 7. Plots of the percent active Si that forms cr-$Li_{15}Si_4$ at full lithiation (*f*) vs cycle number and volumetric capacity vs cycle number of $Si_{90}Mo_{10}$ and $Si_{80}Mo_{20}$ alloy electrodes.

Also listed are the percent volume expansions of these alloys, based on the reversible capacity and calculated according to Ref. 8. As expected, increasing the Mo content results in lower capacity because of the formation of the β-$MoSi_2$ and α-$MoSi_2$ phases, which were found to be inactive (Supporting Information). Reversible and irreversible capacities generally decrease with milling time from 1 h to 4 h and then stabilize after 4 h. This suggests that the reaction between Si and Mo to produce inactive silicides is complete after 4 h milling, which is in accordance with the results of the phase composition analysis of Si–Mo alloys during milling.

Figure 6 shows the 1st, 2nd, 10th and 30th cycle differential capacity (dQ/dV) curves of the Si_xMo_{100-x} electrodes. Sharp peaks observed during the first lithiation indicate a nucleation and growth process during the initial lithiation step.[10] In general, two broad peaks are present in the subsequent lithiation processes, which is typical of a-Si. Sharp peaks at about 0.45 V during delithiation can be clearly observed for $Si_{90}Mo_{10}$ (1–16 h) and $Si_{80}Mo_{20}$ (1 h), which corresponds to the delithiation of cr-$Li_{15}Si_4$, indicating its formation at full lithiation.[27] Broad peaks at about 0.4 V during delithiation also exist in the differential capacity curves of the $Si_{90}Mo_{10}$ (1–16 h) alloys. We have also observed this behavior in Si–Fe–Mn alloys and speculate that the two peaks arise from the different environments of $Li_{15}Si_4$ at the $Li_{15}Si_4$/metal silicide contact region compared to $Li_{15}Si_4$ within the bulk of the $Li_{15}Si_4$ grains.[28]

The amount of cr-$Li_{15}Si_4$ formed during cycling was quantified as the ratio between the delithiation capacity in the 0.36–0.48 V range and the total delithiation capacity, as described in Ref. 28. This ratio is about 0.2 for no cr-$Li_{15}Si_4$ formation and about 1 if all the Si forms cr-$Li_{15}Si_4$ after full lithiation. Therefore, the percent active Si in the alloy that forms the cr-$Li_{15}Si_4$ phase during cycling (*f*) is:

$$f = \frac{\left(\frac{Q_{0.36-0.48\ V}}{Q_{tot}} - 0.2\right)}{1 - 0.2} \times 100\% \qquad [3]$$

Where $Q_{0.36-0.48\ V}$ is the delithiation capacity in the 0.36–0.48 V range and Q_{tot} is the total delithiation capacity. Figure 7 shows the amount of active Si that forms cr-$Li_{15}Si_4$ during cycling vs cycle number for all the $Si_{90}Mo_{10}$ (1–16 h) and $Si_{80}Mo_{20}$ (1–16 h) half cells shown in Fig. 6. Data for the $Si_{70}Mo_{30}$ samples are not shown because they are essentially inactive. It can be seen in Fig. 7 that the Si–Mo alloys with longer milling time and more Mo content show better cr-$Li_{15}Si_4$ suppression. This is shown more clearly in Fig. S6,

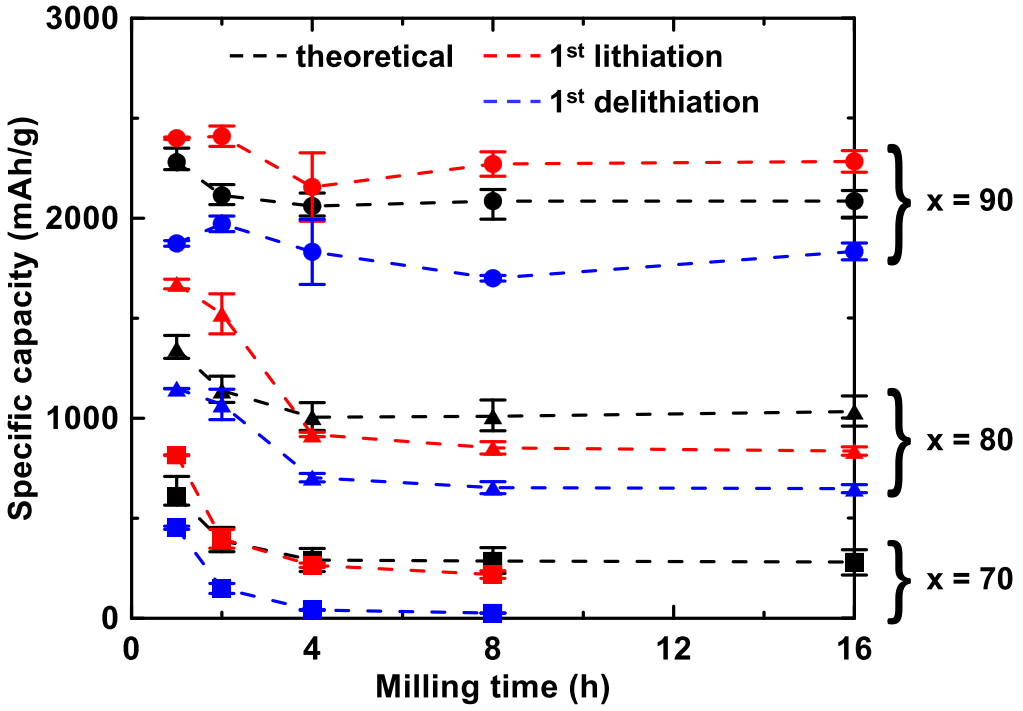

Figure 8. Comparison between the theoretical capacities, 1st lithiation capacities, and 1st delithiation capacities of Si_xMo_{100-x} ($90 \geqslant x \geqslant 70$, $\Delta x = 10$, 1–16 h) alloys.

which shows the maximum value of f plotted as a function of milling time. The enhanced cr-$Li_{15}Si_4$ suppression arises presumably because long milling time and high Mo content contribute to fine gain structure (homogenous Si–Mo distribution) as illustrated in Fig. 4. This is consistent with earlier studies, as increasing milling time reduces Si grain size and increases the Si/inactive phase contact area, while increasing the inactive phase has been shown to suppress the formation of cr-$Li_{15}Si_4$ by shifting the potential profile to lower potentials.[9,10] Indeed, this was found to be the case here, as the average lithiation potentials of the alloys were found to generally decrease with increasing milling time (Fig. S7).

Figure 7 also shows the cycling performance of $Si_{90}Mo_{10}$ and $Si_{80}Mo_{20}$ alloys in terms of volumetric capacity. The specific capacity of $Si_{90}Mo_{10}$, $Si_{80}Mo_{20}$, and $Si_{70}Mo_{30}$ alloys and the volumetric capacity of $Si_{70}Mo_{30}$ alloys are also shown in Fig. S8. As milling time increases more Si is consumed to form the inactive $MoSi_2$ phase, reducing capacity, as mentioned above. The relation between milling time and first cycle capacity is shown in Fig. 8, which also confirms that a steady-state has been reached after 4 h milling. After this reaction is completed (i.e. for samples milled 4 h or more) the capacity remains constant. For these samples both specific and volumetric capacities decrease with increasing Mo content, however the volumetric capacity decreases much less dramatically, since the addition of Mo also increases density.

As shown in Fig. 7, all samples milled 4 h or longer show good capacity retention during the 50 cycles tested, excepting the $Si_{90}Mo_{10}$ samples, which are the samples that also exhibited cr-$Li_{15}Si_4$ formation during cycling. Relationships between cr-$Li_{15}Si_4$ formation, reversible capacity (1st delithiation capacity) and capacity fade are illustrated in Figs. S9a–S9d. As shown in Fig. S9a, the capacity fade of the high capacity $Si_{90}Mo_{10}$ alloys is highly correlated to cr-$Li_{15}Si_4$ formation during cycling. This indicates that these high volume expansion alloys are susceptible to internal fracture when cr-$Li_{15}Si_4$ formation is not suppressed during cycling. In contrast, the lower capacity/volume expansion $Si_{80}Mo_{20}$ alloys have much smaller f values and show no such correlation (Fig. S9b). The high capacity $Si_{90}Mo_{10}$ alloys all show higher levels of fade (Fig. S9c) than the $Si_{80}Mo_{20}$ alloys (Fig. S9d). This higher level of fade is likely related to mechanical disconnection from the electrode during cycling the high capacity alloys. As the capacity becomes lower in the $Si_{80}Mo_{20}$ alloys with greater milling time, the fade correspondingly becomes smaller.

Figure 8 shows the first lithiation capacity, first delithiation capacity and theoretical capacity based on quantitative XRD analysis, assuming that only the Si phase is active, of the Si_xMo_{100-x} ($90 \geqslant x \geqslant 70$, $\Delta x = 10$, 1–16 h) samples plotted as a function of milling time. For the $Si_{90}Mo_{10}$ 1–16 h, $Si_{80}Mo_{20}$ 1–2 h, and $Si_{70}Mo_{30}$ 1 h samples, the theoretical capacities have values between the 1st lithiation and 1st delithiation capacities, as expected. For the $Si_{80}Mo_{20}$ 4–16 h and $Si_{70}Mo_{30}$ 2–8 h samples, the measured capacities are less than predicted theoretically, indicating incomplete lithiation of the active Si phase. This may be due to the encapsulation of some active Si by the larger amount of inactive phase, as shown in Fig. 4.

Selected Si–Mo alloys were heated at 600 °C and 800 °C to study their thermal stability. XRD patterns of selected $Si_{90}Mo_{10}$, $Si_{80}Mo_{20}$, and $Si_{70}Mo_{30}$ alloys before and after heating are shown in Figs. S10–S12, respectively. In general, alloy crystallization, indicated by sharpening XRD peaks, was slight at 600 °C, but became readily evident at 800 °C. The phase evolution during heating is shown in Fig. S13. During heating the Si–Mo 1 h samples, the Mo content decreased, which is indicative of its reaction with Si to produce $MoSi_2$. This shows that after 1 h ball milling, the reaction is not complete. In contrast, the phase behavior of the 4 h and 16 h samples are similar, confirming that the ball milling reaction between Si and Mo is complete after only 4 h. After heating at 800 °C, the crystallization of a-Si occurred in all Si–Mo alloys. In addition, the β-$MoSi_2$ phase converts to the α-$MoSi_2$ during heating at 600 and 800 °C, which is consistent with the Si–Mo equilibrium phase diagram where α-$MoSi_2$ is the stable phase of $MoSi_2$ below 1900 °C.

The grain sizes of the cr-Si and β-$MoSi_2$ phases in all the Si–Mo samples were calculated based on the Scherrer equation and are plotted in Fig. S14 as a function of heating temperature. The grain size of the β-$MoSi_2$ phase grows with heating temperature for all alloys regardless of composition and milling time. For samples milled 4 h and longer, the cr-Si phase that appears at 800°C has

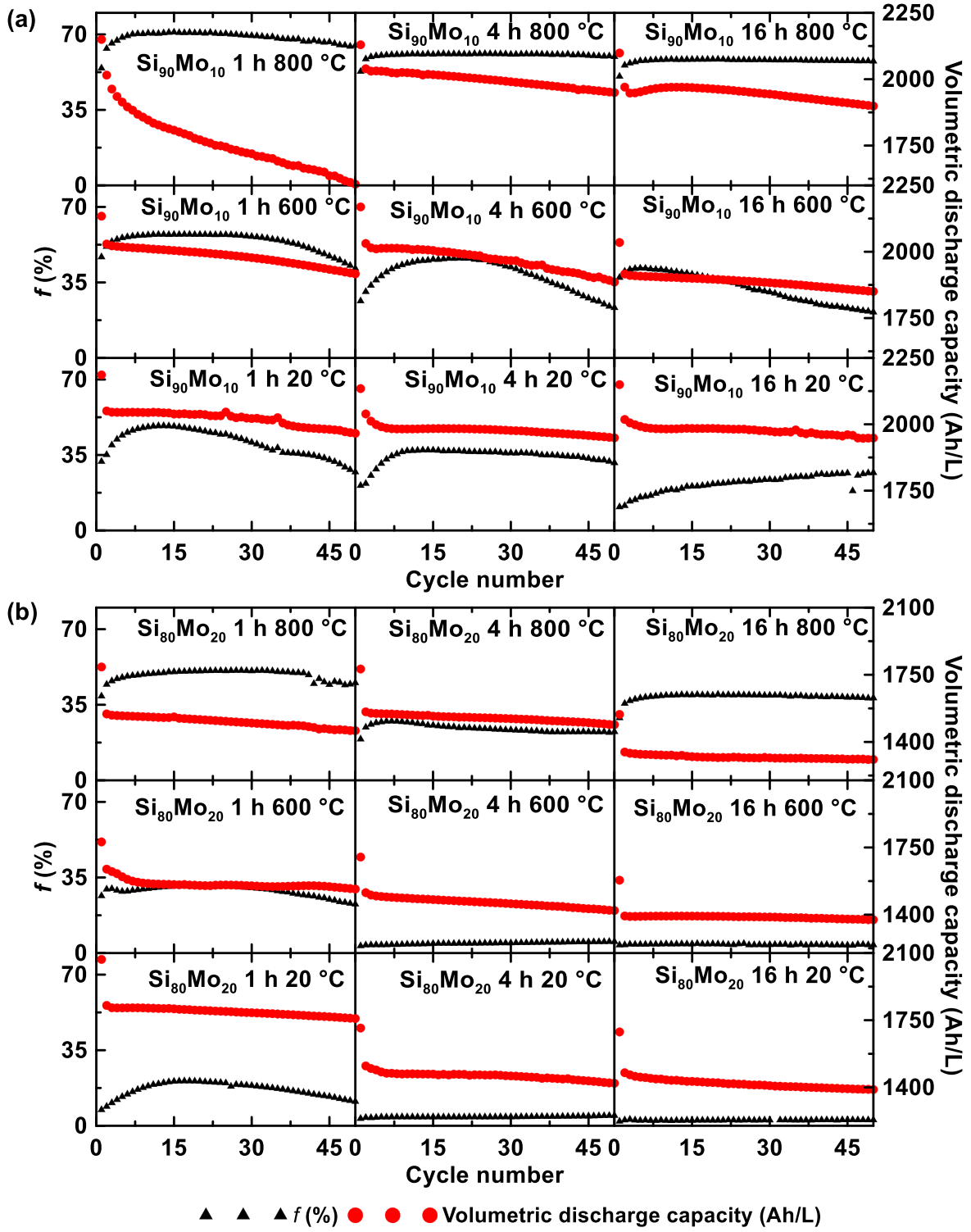

Figure 9. Plots of the percent active Si that forms cr-$Li_{15}Si_4$ at full lithiation (*f*) vs cycle number and volumetric capacities vs cycle number of (a) $Si_{90}Mo_{10}$ and (b) $Si_{80}Mo_{20}$ alloy electrodes with different heat treatment temperatures.

lower grain size when the sample is milled longer. This may result from better dispersion of the Si phase in the alloy (shown in Fig. S1 and Fig. 4). However, Figs. S10–S14 clearly show that $MoSi_2$ fails to suppress Si crystallization at temperatures greater than 600°C and even more readily crystalizes itself, despite its high melting point.

Figure S15 shows the potential profiles (for the first four cycles) of the Si–Mo alloys before and after heat treatment at different temperatures. The consequences of their crystallization during heating are readily apparent. Compared to the unheated Si–Mo alloys, a more pronounced delithiation potential plateau at about 0.45 V is present for the heated sample, indicating a greater degree of cr-$Li_{15}Si_4$ formation. This is likely because of the growth of Si and $MoSi_2$ grains during heating, resulting in their disconnection from the inactive phase and, subsequently, a lack of the suppression of cr-$Li_{15}Si_4$ formation.[29] This can be seen more clearly in Figs. 9a and 9b, which shows the cycling performance (volumetric capacity vs cycle number) and the degree of cr-$Li_{15}Si_4$ formation (*f*) as a function of cycle number for $Si_{90}Mo_{10}$ and $Si_{80}Mo_{20}$, respectively.

The reversible and irreversible specific capacities, ICE, and percent volume expansions of the Si–Mo samples after heat treatment can be found in Table SII. Both the $Si_{90}Mo_{10}$ 16 h and $Si_{80}Mo_{20}$ 16 h samples before and after heat treatment have comparable cycling performance, which shows that these Si–Mo alloys have high temperature tolerance. The heated $Si_{90}Mo_{10}$ 16 h samples have high reversible specific capacities of about 1500–1700 mAh g^{-1} and large reversible volumetric capacities of about 1900–2000 Ah L^{-1}. The heated $Si_{80}Mo_{20}$ 16 h samples have much lower reversible specific capacities about 500–600 mAh g^{-1}, but they still have high volumetric capacities of about 1300–1400 Ah L^{-1}, since these alloys have larger density than $Si_{90}Mo_{10}$ samples.

Figures S9a–S9d show the relationships between cr-$Li_{15}Si_4$ formation, reversible capacity and capacity fade retention affect 10–50 cycle capacity fade of all heated and unheated $Si_{90}Mo_{10}$ and $Si_{80}Mo_{20}$ alloys. The same general trends found for the unheated alloys remain present for the heated alloys. Figures S9a and S9c suggest that the 10–50 cycle capacity fade of the large capacity $Si_{90}Mo_{10}$ alloys largely depends on the cr-$Li_{15}Si_4$ formation fraction during cycling, which is related to internal particle fracture. For the lower capacity $Si_{80}Mo_{20}$ alloys, the capacity fade during 10–50 cycles is less and increases with increasing reversible capacity. This shows that in these lower expansion alloys, fade is mostly affected by the structural integrity of the electrode, rather than particle fracture. Because of this property, good cycling can be achieved in these alloys as long as the reversible capacity is not excessive. This is illustrated in the 16 h milled $Si_{80}Mo_{20}$ alloys heated to 800 °C. Despite being highly crystalline (Fig. S11) and exhibiting large amounts of cr-$Li_{15}Si_4$ formation during cycling (40%), the capacity fade of this sample is the lowest of all of the alloys measured (∼13 mAh g^{-1} or 0.8%/cycles 10–50).

Conclusions

The phase evolution during ball milling, electrochemical properties, and thermal stability of Si–Mo alloys were studied. It was found that Si–Mo can rapidly form nanostructured a-Si/$MoSi_2$ alloys by ball milling within 4 h. However, caking of Mo on the walls of the ball mill occurred during ball milling, especially for high-Mo content alloys, which could be detrimental to manufacturing processes. These alloys were found to have similar thermal stability as other Si-transition metal alloys, with the crystallization of the a-Si phase occurring at about 600 °C and crystallization of the $MoSi_2$ phase occurring at even lower temperatures. This crystallization resulted in a high degree of $Li_{15}Si_4$ formation during cycling. However, surprisingly, this was not found to be detrimental to cycling for the samples heated at 800 °C. Such samples seemed to be able to maintain electrical contact to the active Si phase despite $Li_{15}Si_4$ formation. As a result, Si–Mo alloys can provide good cycling performance at high temperatures despite not being especially thermally stable. The $Si_{90}Mo_{10}$ 16 h and $Si_{80}Mo_{20}$ 16 h alloys after heat treatment at 800 °C also have high reversible volumetric capacities of about 1900 Ah L^{-1} and 1300 Ah L^{-1}, respectively. The compatibility of these alloys with the high temperatures required for the carbon coating process make them good candidates as compositions for highly engineered Li-ion battery anode materials.

Acknowledgments

The authors acknowledge financial support from NSERC, Novonix Battery Testing Services Inc., the Canada Foundation for Innovation, and the Atlantic Innovation Fund for this work.

ORCID

M. N. Obrovac https://orcid.org/0000-0001-5509-3185

References

1. M. N. Obrovac and V. L. Chevrier, *Chem. Rev.*, **114**, 11444 (2014).
2. J. R. Dahn, T. Zheng, Y. Liu, and J. S. Xue, *Science*, **270**, 590 (1995).
3. M. N. Obrovac and L. Christensen, *Electrochem. Solid-State Lett.*, **7**, A93 (2004).
4. I. A. Courtney, J. S. Tse, O. Mao, J. Hafiner, and J. R. Dahn, *Phys. Rev. B*, **58**, 15583 (1998).
5. D. S. M. Iaboni and M. N. Obrovac, *Electrochem. Soc.*, **163**, A255 (2016).
6. H. Lee, Y. Kim, M. Hong, and S. Lee, *J. Power Sources*, **141**, 159 (2005).
7. H. Wu and Y. Cui, *Nano Today*, **7**, 414 (2012).
8. M. N. Obrovac, L. Christensen, D. B. Le, and J. R. Dahn, *J. Electrochem. Soc.*, **154**, A849 (2007).
9. Z. Du, T. D. Hatchard, R. A. Dunlap, and M. N. Obrovac, *J. Electrochem. Soc.*, **162**, A1858 (2015).
10. H. Liu, M. Zhu, Z. Du, and M. N. Obrovac, *J. Electrochem. Soc.*, **163**, A192 (2015).
11. Y. Cao, J. C. Bennett, R. A. Dunlap, and M. N. Obrovac, *J. Electrochem. Soc.*, **165**, A1734 (2018).
12. Y. Wang, S. Cao, M. Kalinina, L. Zheng, L. Li, M. Zhu, and M. N. Obrovac, *J. Electrochem. Soc.*, **164**, A3006 (2017).
13. M. D. Fleischauer, J. M. Topple, and J. R. Dahn, *Electrochem. Solid-State Lett.*, **8**, A137 (2005).
14. M. D. Fleischauer, M. N. Obrovac, and J. R. Dahn, *J. Electrochem. Soc.*, **153**, A1201 (2006).
15. Z. Du, T. D. Hatchard, P. Bissonnette, R. A. Dunlap, and M. N. Obrovac, *J. Electrochem. Soc.*, **163**, A2456 (2016).
16. M. L. Terranova, S. Orlanducci, E. Tamburri, V. Guglielmotti, and M. Rossi, *J. Power Sources*, **246**, 167 (2014).
17. Y. S. Hu, R. Demir-Cakan, M. M. Titirici, J. O. Muller, R. Schlogl, M. Antonietti, and J. Maier, *Angew. Chem. Int. Ed.*, **47**, 1645 (2008).
18. A. Magasinski, P. Dixon, B. Herzberg, A. Kvit, J. Ayala, and G. Yushin, *Nat. Mater.*, **9**, 353 (2010).
19. M. T. McDowell, S. W. Lee, J. T. Harris, B. A. Korgel, C. Wang, W. D. Nix, and Y. Cui, *Nano Lett.*, **13**, 758 (2013).
20. X. H. Liu, L. Zhong, S. Huang, S. X. Mao, T. Zhu, and J. Y. Huang, *ACS Nano*, **6**, 1522 (2012).
21. T. D. Hatchard, A. Genkin, and M. N. Obrovac, *AIP Adv.*, **7**, 045201 (2017).
22. M. Kahle, M. Kleber, and R. Jahn, *Geoderma*, **109**, 191 (2002).
23. L. Zevin, *Accuracy in Powder Diffraction II: Proceedings of the International Conference, 17*, NIST special publication, 846 (1992).
24. A. B. Gokhale and G. J. Abbaschian, *J. Phase Equilibria*, **12**, 493 (1991).
25. Y. Liu, B. Scott, and M. N. Obrovac, *J. Electrochem. Soc.*, **166**, A1170 (2019).
26. J. P. Maranchi, A. F. Hepp, and P. N. Kumta, *Electrochem. Solid-State Lett.*, **6**, A198 (2003).
27. M. N. Obrovac and L. J. Krause, *J. Electrochem. Soc.*, **154**, A103 (2007).
28. Y. Cao, B. Scott, R. A. Dunlap, J. Wang, and M. N. Obrovac, *J. Electrochem. Soc.*, **166**, A21 (2019).
29. S. Cao, J. Bennett, Y Wang, S. Gracious, M. Zhu, and M. N. Obrovac, *J. Power Sources*, **438**, 227003 (2019).